

Lensed Image Angles: New Statistical Evidence for Substructure

Liliya L.R. Williams, Patrick Foley, Damon Farnsworth

*Department of Astronomy
University of Minnesota
116 Church Street SE
Minneapolis, MN 55455*

llrw@astro.umn.edu

and

Jason Belter

*Nova Classical Academy
1668 Montreal Ave
St. Paul, MN 55116*

ABSTRACT

We introduce a novel statistical way of analyzing the projected mass distribution in galaxy lenses based solely on the angular distribution of images in quads around the lens center. The method requires the knowledge of the lens center location, but the images' distances from the lens center are not used at all. If the images of a quad are numbered in order of arrival time, θ_1 through θ_4 , and θ_{ij} is the angle between images i and j , then we define the 'bisector' plane whose axes are linear combinations of θ_{23} and θ_{14} . The bisector plane of a given lens contains all the quads produced by the lens. We show empirically that all two-fold symmetric lenses with convex, i.e. non-wavy or petal-like isodensity contours are identical in the bisector plane of their quads. We also study lenses with twisting isodensity contours, lumpy substructure, etc. Our results suggest that to reproduce the general characteristics of the observed quad population, kpc-scale substructure must be a common feature of galaxy lenses.

Subject headings: gravitational lensing

1. Introduction

In the last decade or so gravitationally lensed QSOs, both doubles and quads, have been used mostly for the determination of the Hubble parameter (see Coles (2008) for the latest work, and summary of earlier results), and for the estimation of the mass distribution in the lensing galaxies. In this paper we will concentrate on the latter.

One can loosely divide the information on the lens mass distribution into two categories: radial and angular. Much attention has been paid in the literature to the sky-projected radial mass distribution in lenses because the slope of the density profile, and its variation with radius is a test of cosmological models (Navarro et al. 1996, 1997). The density profile slope in the central regions is also important because it is affected by the (adiabatic) contraction of dark matter halos in response to the collapsing baryons during galaxy formation (Ferreras, et al. 2005, 2008; Grillo et al. 2008).

The angular distribution of lensing mass, for example, the degree of ellipticity, the change in the ellipticity position angle with radius, etc. have received some attention as well (Corless et al. 2008; Saha & Williams 2006; Oguri & Keeton 2004), but mostly as “nuisance” parameters in determining the radial density profile or the Hubble constant. It is somewhat ironic that the generally uninteresting ellipticity position angle can be unambiguously estimated by any reasonable modeling method, even by eye (Saha & Williams 2003), whereas, the more interesting density profile slope is often very uncertain because of the mass-sheet, or steepness degeneracy (Falco et al. 1985; Saha 2000).

The positions of lensed images of a quad or a double can also be looked at as consisting of angular and radial information. By radial information we mean the relative spread of images in distance from the lens center. The angular information is the angular separation of the images as viewed from the lens center. For example, in the Cloverleaf, H1413+117, and the Einstein Cross, Q2237+030 any two adjacent images are roughly 90° apart. In doubles, the two non-central images tend to be separated by $\sim 150^\circ - 180^\circ$.

Obviously there is no simple one-to-one relation between, say, the radial structure of the lensing mass and the radial distribution of lensed images. However, there are some qualitative connections between the two. For example, a steep lens mass distribution tends to produce quads with narrow radial spread of images, largely independent of the angular distribution of these images, or the ellipticity of the lensing mass. Conversely, if the lensing mass has a shallow density profile the images tend to have a wider radial spread. In the Appendix of this paper we show that one angular property of the lensing mass, its ellipticity position angle can be straightforwardly and rather precisely estimated from the angular positions of the four images of the quad (Section A).

The main work presented in this paper is loosely motivated by the preceding paragraph. Specifically, we ask what information about the lensing mass can be retrieved by looking solely at the angular distribution of lensed images around the lens center.

2. Defining angles and bisector rays

Following Saha & Williams (2003), we refer to the four images of a quad by their arrival time, as 1, 2, 3, 4. Image 1 is the global minimum of the arrival time surface and hence is the first arriving image. Image 2 is the second arriving image, and is also a minimum. Images 3 and 4 are saddles of the arrival time surface. Image 5, a maximum, is the central demagnified image, and is usually not detected. (See Figure 1). As explained in Saha & Williams (2003) figuring out the arrival *order* of images in observed quads can be done, in most cases, based on the morphology of the image distribution alone, without measuring the time delays.

Images 2 and 3 (minimum and saddle) often appear close together; these are the two images that merge and disappear when the source moves away from the lens center. Because of that, the angular separation of these two images (as seen from the lens center), which we will call θ_{23} can be a measure of the "quadrupoleness" of a quad system. When 2 and 3 are close together the system is barely a quad, and could have been a double if the source happened to be somewhat further away from the lens center, whereas a quad with images 2 and 3 about 90° apart is a "well established" quad.

We also define β_{12} , as the ray anchored at the lens center that bisects the angle between images 1 and 2. If we further specify that β_{12} points roughly away from image 4, then the definition of β_{12} is unambiguous. Similarly, we define β_{34} as the ray bisecting the angle between images 3 and 4, and pointing roughly away from image 1. The two lower panels in Figure 1 show both these rays for a synthetic mass distribution, whose projected density contours are shown in the upper left panel. The images are filled circles. The arrival time surface is shown in the upper right. The lower left panel shows that the images are found as the intersection of the solution of the lens equation in the x and y directions, shown by thick (red) and thin (blue) curves, respectively. The lower right panel shows the source plane caustics, the source position (empty green circle), and the two bisector rays.

These angles and bisector rays turn out to have some very interesting properties, which relate to certain aspects of the lens mass distributions.

3. Mass distribution: Lenses with two-fold symmetry

3.1. Defining two-fold symmetric lenses

A two-fold symmetric lens is a projected mass distribution that has two orthogonal axes of bilateral symmetry. A wide class of popular lens models are two-fold symmetric. For example, this category includes elliptical lenses, with any radial density profile. The degree of ellipticity can be a function of radius, but the ellipticity position angle (PA) should not change with radius. Lenses with single or multiple external shear axes, as long as the shear axes are arranged so as to obey the symmetry, also belong in this category. Two lens classes commonly used for parametric modeling, Pseudo Isothermal Elliptical Mass Distributions (PIEMD) and Pseudo Isothermal Elliptical Potentials (PIEP) (Kassiola & Kovner 1993) are also members of the two-fold symmetric family of lenses.

We exclude lenses that, even though two-fold symmetric, have 'wavy' isodens. (Isodens are contours of equal projected surface mass density in the lens.) For example, lenses whose isodens follow $\cos(2n\theta)$, with $n > 1$, or where isodens look like petals. In other words, mass distributions with non-convex isodens are excluded. This is further discussed in Section 3.3. The mass distributions thus defined will be referred to as two-fold symmetric.

In this paper we examine mass distributions through the properties of the quad lenses they generate. Our study is statistical in nature; we use the properties of the entire quad population produced by a given mass distribution. Insights gained from this study help to draw conclusions from the real data, where a given galaxy lenses one, or maybe a small handful of sources.

In this Section we discuss two-fold symmetric lenses and show that members of this family are indistinguishable when viewed in a diagnostic plane whose axes are certain combinations of image angles. Next, we discuss this diagnostic 'bisector' plane.

3.2. Introducing the bisector plot

The lower right panel of Figure 1 suggests that the axes containing β_{12} and β_{34} are good indicators of the orientation of the diamond caustic, and by extension, the PA of the major and minor axes of the lensing mass distribution around the image ring. This statement is quantified in the Appendix; here we use this observation to motivate our choice of $\beta_{12} - \beta_{34}$ as an angle that contains useful information about the lensing mass.

In the main portion of Figure 2 (upper right panel) we plot $\beta_{12} - \beta_{34}$ vs. θ_{23} . Each

(red) dot represents a 4-image lens configuration (a quad); all the dots arise from the same galaxy, but each dot has a different source position, picked randomly on the source plane. (Sources that do not produce quads did not make it into this plot.) The galaxy lens used here has an “isothermal” projected density profile $\Sigma(R) \propto R^{-1}$ with a small core to avoid central singularity. The ellipticity, $\epsilon = 0.2$, is constant with radius. (The relation between ϵ and the axis ratio, r is, $\epsilon = [1 - r]/[1 + r]$.)

We call the distribution of points in the $\beta_{12} - \beta_{34}$ vs. θ_{23} plane, the bisector plot. The first thing to note is that the distribution of points in the bisector plot is not random. There are no quads with the bisector difference less than 90° . More interestingly, there is a well defined envelope, a curved line above and to the right of which there are no quads. We will call this the ‘envelope’.

The bisector plot of Figure 2 is flanked by two panels. The solid line histogram in the left side panel shows the distribution of bisector plot points along the θ_{23} direction; the $\beta_{12} - \beta_{34}$ values have been “marginalized” over. The solid line histogram in the bottom panel is the distribution of $\beta_{12} - \beta_{34}$ values; here, the θ_{23} values have been marginalized over. These two histograms do not fully quantify the distribution of points in the main two-dimensional bisector plot, but they do give us an easy, though incomplete way of examining that distribution. As an example consider a hypothetical quad lens at $(100^\circ, 60^\circ)$. When projected on to the two histograms the point falls in the middle of both the distributions. So, if one is to ask if this point could have been drawn from the two distributions, the answer would be ‘yes’ in both cases. However, looking at the full 2-d bisector plane it is obvious that the quad cannot be generated by this lens, as it lies above the bounding envelope, well outside the distribution.

3.3. The bisector plot: an invariant property?

In the previous section we looked at the bisector plot of one type of lens, with a certain density profile and certain ellipticity. We have also generated bisector plots for many types of lenses, with varying density profiles, varying degrees of ellipticity, including ellipticity $\epsilon(r)$ which changes in radius, lenses with and without external shear, etc. Our numerous experiments suggest that *all lenses that possess two-fold symmetry, regardless of the radial density distribution and the magnitude or radial dependence of ellipticity and external shear generate the same distribution of points in the bisector plot, bounded by a vertical line and a concave envelope.* We conclude that all two-fold symmetric lenses, as defined in Section 3.1 are indistinguishable in the bisector plot. This is one of the main findings of this paper.

This invariance must derive from the shape of the caustic in the source plane. From our experiments we have noticed that the inner (five image) caustics of all two-fold symmetric lenses are diamond-shaped, and appear to share the following two features. First, the diamond caustic itself has two-fold symmetry (and so the two lines connecting the opposite cusps are perpendicular to each other), and second, the diamond caustics of any two such lenses can be made to have the same shape if one is allowed to linearly stretch or shrink them in the directions along the lines connecting the opposite cusps. By symmetry arguments, the first feature seems natural for lens mass distributions that have two-fold symmetry. The lines connecting opposite cusps of the diamond caustic of a lens with no such symmetry, for example the one shown in Figure 1 (lower right panel), do not intersect at right angles. The second feature implies the invariance of the caustic itself (modulo linear stretching of the x or y coordinates), and is probably the crux of the bisector plot invariance shown in Figure 2.

The invariance does not extend to lenses that have ‘wavy’ isodens; such lenses tend to produce caustics more complicated than diamond shapes.

The invariance does not apply to lenses with naked cusps, i.e. lenses whose diamond caustic cusps stick outside of the oval caustic because of large ellipticity in the mass distribution.

3.4. The bisector plot envelope for a specific lensing potential

The set of quads that delineate the upper bounding envelope of the bisector plane, shown, for example in Figure 2, must correspond to a continuous set of sources in the source plane of any two-fold symmetric lens. We speculate, and confirm using experiments with synthetic lenses, that the envelope quads, when mapped back to the source plane, form a straight line that connects the center of the lens to the point on the diamond caustic closest to the center; we call this the point of closest approach, and denote it \vec{r}_c .

If the bisector plane is indeed universal, as we claim, then the envelope must be described by a universal analytical expression. Here we derive the equation for the envelope for a specific type of a two-fold symmetric lens.

We start with a lensing potential of the form, $\phi(r, \theta) = r f(\theta)$ (Witt, Mao & Keeton 2000), and work in cylindrical coordinates on the plane of the sky. The arrival time surface is, $\psi(r, \theta) = \frac{1}{2}|\vec{r} - \vec{r}_s|^2 - \phi(r, \theta)$. The lensing equation, $\vec{\nabla}\psi = 0$, in the \hat{r} and $\hat{\theta}$ directions is written as,

$$r_s \cos(\theta - \theta_s) = r - f, \quad r_s \sin(\theta - \theta_s) = \frac{\partial f}{\partial \theta} \quad (1)$$

Using these, the square of the distance of the source from the lens center is,

$$r_s^2 = (r - f)^2 + \left(\frac{\partial f}{\partial \theta}\right)^2, \quad (2)$$

The determinant of the magnification matrix for our lensing potential is,

$$\det A = \frac{1}{r} \left[(r - f) - \frac{\partial^2 f}{\partial \theta^2} \right] \quad (3)$$

For sources on the caustic, $\det A = 0$, and so $r - f = \partial^2 f / \partial \theta^2$. The caustic equation becomes

$$r_s^2 = \left(\frac{\partial^2 f}{\partial \theta^2}\right)^2 + \left(\frac{\partial f}{\partial \theta}\right)^2. \quad (4)$$

The two lensing equations, eq.1 can then be rewritten as,

$$r_s \cos(\theta - \theta_s) = \frac{\partial^2 f}{\partial \theta^2}, \quad r_s \sin(\theta - \theta_s) = \frac{\partial f}{\partial \theta}. \quad (5)$$

Equations 4 and 5 make it apparent that the caustic is oval shaped in the plane defined by orthogonal axes equal to the second and first derivatives of f with respect to θ , respectively. The angle that specifies position in that plane is $(\theta - \theta_s)$. This oval is illustrated in Figure 3, with filled points, and the right and upper axes. Note that this plane, where the caustic has an oval shape is not same as the source plane. For comparison, the caustic in the source plane is also shown in Figure 3, with empty points, and the left and lower axes. In the source plane the caustic has the usual diamond shape. The point of closest approach belongs to the oval and is either on the $\frac{\partial^2 f}{\partial \theta^2}$ axis, or on the $\frac{\partial f}{\partial \theta}$ axis, i.e. either $\frac{\partial f}{\partial \theta} = 0$, or $\frac{\partial^2 f}{\partial \theta^2} = 0$, respectively.

To proceed further we specify the form of ϕ ,

$$\phi(r, \theta) = br(1 + \gamma \cos 2\theta), \quad (6)$$

where b and γ are constant for any given lens. This is the lensing potential of a singular isothermal sphere with an added elliptical perturbation, γ , which generates shear. If there were no shear, b would be the Einstein ring radius of the SIS lens. This SIS+elliptical lens model is discussed, for example in Dalal (1998). For this lens,

$$\frac{\partial^2 f}{\partial \theta^2} = -4b\gamma \cos 2\theta, \quad \frac{\partial f}{\partial \theta} = -2b\gamma \sin 2\theta, \quad (7)$$

which implies that the point of closest approach corresponds to $\frac{\partial^2 f}{\partial \theta^2} = 0$. (This is shown as the solid line segment in Figure 3.) From the first of equations 5, and restricting ourselves

to the 1st and 4th quadrants (the other two are redundant because of symmetry) we derive that $\theta - \theta_c = \pi/2$, $\theta = \pi/4$, and so $\theta_c = -\pi/4$. Here, θ is the lens plane angle of only one of the images. θ_c is the angle of the point of the closest approach, \vec{r}_c in the source plane, which is shown as the dashed line segment in Figure 3 (left and lower axes refer to the source plane).

According to our hypothesis all the points defining the bisector plot envelope lie on a straight line. Therefore, having found its angle, namely θ_c we can now solve for the source positions themselves. To do this we use the second of equations 5. Squaring it, and using $\sin^2 \theta_c = \cos^2 \theta_c = \frac{1}{2}$ we get,

$$\frac{1}{2} \left[\frac{r_s}{2b\gamma} \right]^2 (1 - \sin 2\theta) = \sin^2 2\theta \quad (8)$$

Here, θ refers to any one of four images, two minima and two saddles, and in fact this quadratic equation does have four solutions. There are two solutions for $\sin 2\theta$ from the quadratic itself, and each one of these gives two solutions because $\cos 2\theta = \pm \sqrt{1 - \sin^2 2\theta}$.

The two images with $\sin 2\theta > 0$ are in the 1st and 2nd quadrants, while the other two are in the 3rd and 4th. For each of these two pairs of images their x -coordinates place them equidistantly on either side of the y -axis. This implies that the angular distribution of the four images is symmetric about the y -axis. We can take advantage of this in determining how to sort these 4 images in order of arrival time. First note that images 2 and 3 are interchangeable; the same is true for images 1 and 4. Images 2 and 3 are the ones that merge together when the source is on the caustic. This happens for the largest possible r_s , i.e. $r_c = 2b\gamma$. By considering various pairs of adjacent images in turn, one can show that of the 4 images the two that satisfy the merging criterion are the ones with $\sin 2\theta = (\Delta + K)/2$, where $\Delta = \sqrt{K^2 + 4K}$, and $K = \frac{1}{2}[r_s/r_c]^2 = \frac{1}{2}[r_s/2b\gamma]^2$. When the source is on the caustic $2\theta = -\pi/2$ for both of these. The other two images have to be 1 and 4. The angular separation between images 2 and 3 is then

$$\theta_{23} = \pi/2 - \tan^{-1} \left[\frac{(\Delta + K)/2}{\sqrt{1 - \frac{(\Delta + K)^2}{4}}} \right]. \quad (9)$$

Similarly, the angular separation between images 1 and 4, which is always greater than $\pi/2$ is,

$$\theta_{14} = \pi/2 + \tan^{-1} \left[\frac{(\Delta - K)/2}{\sqrt{1 - \frac{(\Delta - K)^2}{4}}} \right]. \quad (10)$$

Then, with some angle visualizing one arrives at the bisector angle difference as,

$$\beta_{12} - \beta_{34} = [2\pi - (\theta_{23} + \theta_{14})]/2 \quad (11)$$

This is what is plotted as the solid curve in Figure 2, and subsequent similar figures.

4. Real quads

Our quad lenses are taken from the CASTLeS data set (Kochenek et al. 2008). We used all quads, except, PMNJ0134-0931, whose lensing galaxy’s position is ambiguous; B0128+437, whose lens center is unknown; SDSS1406+6126, which has partial data; and Q0047-2808, SDSS1029+2623, SDSS1402+6321 which have no data at all. We also used two lenses that are not in CASTLeS: SDSS J125107.57+293540.5 (Kayo et al. 2007), and HE1113-0641 (Blackburne et al. 2007). Cluster lens SDSS J1004+4112, with QSO image separation of $\sim 15''$ was excluded because the images are formed by the central part of a galaxy cluster, not a galaxy. The source in B1933+503 is a double lobed radio source, whose core and one of the lobes are each lensed into quads. These two quads were included as two separate lenses. This gives us a total of 26 quad lenses listed in Tables 1 and 2. Lenses in Table 1 have unambiguous arrival time ordering of images.

In some cross-like quads it is hard to know what the correct numbering of images should be. In the most ambiguous cases we can only be certain that images 1 and 2 should lie across from one another, and so should images 3 and 4. Using this as the only rule gives us four distinct $(\beta_{12} - \beta_{34}, \theta_{23})$ pairs. However, two of these have unrealistically large θ_{23} values, generally in excess of 100° , and can therefore be discarded, leaving us with two possibilities for the $(\beta_{12} - \beta_{34}, \theta_{23})$ pair. There are 10 ambiguous lenses, and each one generates two lines in Table 2.

The quad data is shown in the bisector plot of Figure 4. The unambiguous arrival time order lenses are represented by bold star symbols. Each one of the 10 ambiguous time order lenses is represented by two smaller star symbols, connected by a thin line.

It is apparent from Figure 4 that the real quads are not drawn from the quad distribution generated by two-fold symmetric lenses. This is most clearly seen close to the ‘apex’ of the bisector plot, near $(\beta_{12} - \beta_{34}, \theta_{23}) = (90^\circ, 90^\circ)$. Here, nearly all star symbols lie outside of the apex outlined by two-fold symmetric lenses. The lower portion of the two-fold symmetric lens bisector plot, roughly below $\theta_{23} \approx 60^\circ$ also appears to be inconsistent with the observed quad population: the latter are distributed more or less evenly in the region below the envelope, whereas the density of small points (from two-fold symmetric lenses) in Figure 2 increases sharply as one approaches the envelope from below. The final major difference is that there is an apparent dearth of real lenses with $\theta_{23} \sim 50^\circ$, which is not reproduced in the two-fold symmetric lenses.

The two solid line histograms in (the two side panels of) Figure 4 represent two-fold symmetric lenses, while the histogram delineated with star symbols are the quad data. The Kolmogorov-Smirnov (KS) test as applied to the θ_{23} distribution states that the real quads

could not have been drawn from the two-fold symmetric lenses at 95% confidence level. The main reason for this is the lack of real quads with θ_{23} around 50° , exactly where the two-fold symmetric lenses predict most of the quads to lie.

The KS test applied to the $(\beta_{12} - \beta_{34})$ distribution is far less conclusive, but note that the KS test is not the optimal test here. In Section 3 we saw that no strictly two-fold symmetric lens can produce $(\beta_{12} - \beta_{34})$ even a degree smaller than 90° . So the presence of real quads with $(\beta_{12} - \beta_{34}) \sim 85^\circ$ rules out these lenses. We conclude that the population of real quads could not have been generated by two-fold symmetric galaxy lenses only. Many lensing galaxies must have more complicated mass distributions.

In the next section we explore lenses with twisting isodens and lenses with various degrees of substructure. That substructure may be important is already suggested by HE0230. This lenses' image time ordering is unambiguous. Its coordinates in the bisector plot of Figure 4 are at approximately $(116^\circ, 41^\circ)$, quite far above the envelope. According to the arguments of Section 3, the lens mass distribution must deviate strongly from two-fold symmetric. And in fact, looking at the optical image of the lens (see CASTLeS) it is apparent that in addition to the main lensing galaxy there is a secondary galaxy, located close to image 4. The spectroscopic data of (Eigenbrod et al. 2006) shows that the main lensing galaxy and the smaller secondary one are most probably members of a galaxy group. A tentative conclusion, to be tested in the next section, is that lens substructure in HE0230 and other lenses is responsible for the disagreement between the bisector plots of two-fold symmetric lenses and the real quad population.

5. Mass distribution: Lenses lacking two-fold symmetry

This is a large class of lens models, for example, lenses with twisting density contours, lenses with internal and external shear of different amplitudes and PAs, lenses with substructure, etc. Many real lenses belong in this vast category.

As a first example we take a synthetic galaxy lens with highly twisting isodens, the one shown in Figure 1, and also in the lower left inset in Figure 5. The thick (blue) contour has the surface mass density equal to critical for lensing. The main portion of the same figure is the bisector plot. The single peak of Figure 2 has now split into two peaks. The upper right inset in a plain line box shows the source plane caustics. In contrast to the caustics of two-fold symmetric lenses, this diamond caustic is not two-fold symmetric, for example, the lines connecting its opposite cusps are not perpendicular to each other.

The left and bottom side panels of Figure 5 show, in bold, the θ_{23} and $\beta_{12} - \beta_{34}$ histograms

for this lens. As in the case of two-fold symmetric lenses, the real quad θ_{23} distribution does not match that of the synthetic lens with twisting isodens, because the latter peaks, instead of dipping around 50° .

The mass distribution of the Figure 5 lens was not meant to represent any real projected galaxy. Isoden twists in real galaxies result from the projection of intrinsically triaxial galaxies with radially dependent axes ratios. To produce a more realistic isoden twisting we start with a three dimensional mass distribution given by,

$$\rho(r) = (1 + r/r_0)^{-2}, \quad \text{and} \quad r^2 = \frac{x^2}{a^2} + \frac{y^2}{b^2/t} + \frac{z^2}{c^2/t}, \quad (12)$$

where t , a parameter proportional to x , governs the rate of change of axis ratios with radius. We used $a : b : c = 1 : 10 : 2$. Projecting this triaxial galaxy on to the plane of the sky using Euler angles $\phi = 30^\circ$, $\theta = 40^\circ$ and $\psi = 100^\circ$ we get the mass map shown in the lower left inset of Figure 6. The normalization of the mass distribution is such that the thick (blue) contour has the critical surface mass density for lensing. The difference in the PA of the inner and outer isodens is about 70° , consistent with what is observed for nearby galaxies (Lauer et al. 2005). For our purposes, this synthetic galaxy is a reasonable approximation for a typical projected triaxial galaxy.

Sampling the source plane caustic, shown in the upper right inset, using randomly placed sources we get the main panel of Figure 6. This bisector plot looks similar to the one in Figure 5, only the separation of the peaks around $\beta_{12} - \beta_{34} = 90^\circ$ is smaller. In general, the spread of the peaks is directly related to the degree of isoden twisting in the lens. Just as in the case of Figure 5, this lens model, and by extension the population of realistic triaxial galaxies cannot reproduce the bisector plot distribution of the real quads, primarily because of the dearth of observed quads with θ_{23} near 50° .

Before we leave lenses with twisting isodens we note that elliptical lenses with external shear whose axis does not coincide with the PA of the lens produce bisector plots similar to the ones in Figures 5 and 6.

Next, we turn to lenses with substructure lumps, like secondary or satellite galaxies located close the primary lens galaxy. Our goal here is to consider a few representative substructure types. A systematic exploration of the substructure and what matches observations best will be done in a later paper. Figures 7 and 8 show results for lenses with one subclump each. In the first case, Figure 7, the subclump represents a small perturbation to the lens, so the caustic is only slightly distorted from its two-fold symmetric diamond shape. Because the lens is now more complex, the bisector plot is also more complex. However, the θ_{23} distribution still does not look like that of the real quads.

In the second case, Figure 8, the subclump is compact and relatively more massive. Here, the lens’ θ_{23} distribution (left side panel) looks quantitatively different from all the ones we have considered so far; it is not a single peaked distribution, centered at about 55° . The main peak has moved to 40° , and there is an incipient second peak close to $\theta_{23} = 90^\circ$. Furthermore, the bisector plot points are beginning to extend far above the envelope, almost reaching HE0230, the ‘outlier’ at $(116^\circ, 41^\circ)$. Perhaps it is not surprising that this lens model (almost) reproduces HE0230; the lens model contains a major secondary perturber, just as the real lens in the HE0230 system.

Figure 9 shows the results for a lens with two substructure clumps. The caustic bears no resemblance to a diamond shape, and the bisector plot distribution is very complex. This lens model reproduces, at least qualitatively, major features of the observed quad distribution in the bisector plane. Note that we did not aim to do so; no effort was put into matching the observed distribution in any detail. The dearth of quads at $\theta_{23} \sim 50^\circ$ is present in the synthetic lens, and the distribution of points in the bisector plane extends all the way to HE0230, something that even the lens of Figure 8 could not do.

Figures 6–9 are meant only as qualitative guides to different types of non two-fold symmetric lenses. Based on these we tentatively conclude that the real population of quad lenses requires lumpy substructure; features like twisting isodens and external shear are not enough. However, a thorough exploration of the parameter space of lenses is needed to make robust conclusions. This will be the subject of a later paper.

6. Real doubles

As the source of a quad system moves further away from the lens center images 2 and 3 move closer to each other, and closer to the critical line, and eventually disappear, transforming the lens into a double. As a quad turns into a double, $\theta_{23} = 0$ and the remaining images, 1 and 4, become the two images of a double. Figure 2 tells us that the largest bisector difference in a quad is 120° . Combining this with eq. 11 tells us that “newly formed” doubles should have $(2\pi - \theta_{14})/2 = 120^\circ$, i.e. their image separation should be at least $\theta = 120^\circ$. So, there should be no doubles with image separation $< 120^\circ$. If the lens is not two-fold symmetric this limiting angle can change a little.

Because doubles have only two images there is no such thing as a bisector plot for doubles, however, one can make a plot equivalent to the bottom panels of Figures 2-9. This is shown in Figure 10. The thick solid line histograms the angle between the two images of 39 doubles taken from CASTLeS. As expected, the angle between the two images generally

stays above 120° .

The other four histograms in Figure 10 represent synthetic lenses. The two thin solid line histograms correspond to galaxy lenses whose projected density profile is proportional to $\exp(-R^{0.25})$. The two dashed histograms represent “isothermal” lenses with a small core; outside the core the projected density scales as R^{-1} . Each one of these density profiles was given two, constant in radius, ellipticities: $\epsilon = 0.1$ (axis ratio, $r = 0.82$) and $\epsilon = 0.2$ (axis ratio, $r = 0.67$). Each one of the two shallower lenses were given the same ellipticities. The ellipticities are labeled in the plot. All four synthetic lenses are two-fold symmetric, but, in contrast to the quads, the distributions of these lenses in the equivalent $\beta_{12} - \beta_{34}$ are different.

The conclusion we draw is that the distribution of doubles in angles is a more complex function of the galaxy lens parameter than is the case for quads. A more detailed exploration of the doubles distribution in angles, perhaps coupled to the analysis of the quads, will be a subject of another paper.

7. Summary and Conclusions

We introduce a novel way of analyzing the projected mass distribution in galaxy lenses that relies on the angular distribution of images in quads and doubles around the lens center. If the images of a quad are numbered in order of arrival, as θ_1 , through θ_4 , and θ_{ij} is the angle between images i and j then we define the bisector plane whose axes are linear combinations of θ_{23} and θ_{14} . We show empirically that all two-fold symmetric lenses with convex isodensity contours are identical when considered in the bisector plane. We derive an analytical expression for the boundary envelope of the allowed region, for a specific type of lens. These results concerning the invariance of the bisector plane for two-fold symmetric lenses is one of the main findings of the paper. It means, for example, that from the point of view of θ_{23} and θ_{14} of quads, a Pseudo Isothermal Elliptical Mass Distribution is identical to a circular lens, with any density profile plus an external shear.

This invariance of the bisector planes of two-fold symmetric lenses can be used to examine the structure of the real galaxy lenses. We conclude that the observed quad population was not produced by two-fold symmetric lenses.

We also look at three realistic types of non two-fold symmetric mass distributions, (1) galaxies with twisting isodensity contours, and elliptical galaxies with external shear axis, (2) galaxies with single substructure clumps, and (3) galaxies with two substructure clumps. It appears that only the last type of lenses is able to reproduce the real quad population.

This of course does not mean that all galaxies with observed quads are of type (3), but it does suggest that kpc-scale substructure is a common feature in galaxy lenses.

To confirm and quantify this conclusion a much more detailed exploration of the parameter space of non two-fold symmetric lenses is needed. Such a study should also include potential sources of bias in the quads. For example, in this paper we have assumed that the real lenses represent a random sampling of the relevant region in the source plane; in other words, all sources have the same weights. This means that we have neglected magnification bias, which makes sources at certain source plane locations more magnified, and hence more likely to enter a magnitude limited sample. The bias is probably negligible for quads, since they are already highly magnified; after all, quads are closely related to Einstein rings. It is unlikely that there is a missing population of faint quads. However, the magnification bias could be an issue for the doubles, and will need to be taken into account in future work.

Two final notes are in order. First, the lumpy substructure we refer to here is different from that searched for using image flux anomalies, e.g. Mao et al. (2004). In the latter case substructure lumps are small, and have to lie close to the line of sight to the images. Our substructure lumps are larger, kpc-sized, more extended and can live anywhere within the central several kpc of the galaxy lens center. Second, the varied and complex lumpy substructure that our analysis implies the lenses should have argues strongly for using non-parametric, or semi-parametric modeling techniques.

This work was supported in part by NSF grant AST 03-07604, and HST-AR-10985.01-A.

A. Estimating the PA of the lens’ major axis

A given lens system can produce a variety of image configurations, depending on the location of the source. The four panels of Figure 11 show the same lens galaxy with four different source positions. As the source location changes the angular positions of the images, and their angular separation also change considerably. However, the axis containing the bisector rays β_{12} and β_{34} change very little (i.e. β_{12} and β_{34} modulo π). Furthermore, the axes containing β_{12} and β_{34} coincide with the major and minor axes of the diamond caustic, respectively, to within $\sim 10^\circ$.

Figure 12 this observation; it histograms the angle containing the β_{12} . Because this can be either β_{12} or $\beta_{12} + \pi$ the full possible range is π . Each point contributing to the histogram represents a random source position. The thick down-arrow indicates the actual PA of the major axis of the diamond caustic. This is very nearly the same as the mode (peak of the

histogram) and the median (central thin arrow) of the β_{12} distribution. The other two thin arrows mark the 10th and 90th percentiles. The half-width of the β_{12} distribution is about 7° , i.e. the axis containing β_{12} is $\pm 7^\circ$ from the true PA of the major axis of the diamond caustic. This means that for an unknown position of the source, measuring the axis of β_{12} and equating it to the axis containing the cusps of the caustic will typically result in a 7° error, or, fractional error of about 4%.

In the absence of strong external shear the direction of the major axis of the diamond caustic is aligned with the major axis of the mass distribution in the ring of the images. Therefore the PA of the axis containing bisector β_{12} is aligned with the major axis of the mass distribution at the radius of the images. In Saha & Williams (2003) we noted that the direction of the dominant shear or ellipticity in a lens can be determined from the images: The images lie on an eccentric ellipse whose major axis is perpendicular to the major axis of the dominant shear (whether it is internal or external). Here we suggest a more precise measure of the direction of the mass ellipticity, namely, the axis containing β_{12} .

REFERENCES

- Blackburne, J.A., Wisotzki L., & Schechter, P.L. 2007, <http://arxiv.org/abs/0710.3593>
- Coles, J. 2008, preprint, <http://arxiv.org/abs/0802.3219>
- Corless, V.L., Dobke, B.M., & King, L.J., <http://arxiv.org/abs/0804.0692>
- Dalal, N. 1998, ApJ, 509, L13
- Eigenbrod, A., Courbin, F., Meylan, G., Vuissoz, C., Magain, P. 2006, A&A, 451, 759
- Falco, E. E., Gorenstein, M. V. & Shapiro, I. I. 1985, ApJ, 289, L1
- Ferreras, I., Saha, P. & Williams, L.L.R. 2005, ApJ, 623, L5
- Ferreras, I., Saha, P. & Burles, S.
- Grillo, C., Gobat, R., Rosati, P. & Lombardi, M. 2008, A&A, 477, L25
- Kassiola, A. & Kovner, I. 1993, ApJ, 417, 450
- Kayo, I. et al. 2007, <http://arxiv.org/abs/0707.2651>
- Keeton, C.R., Gaudi, B.S. & Petters, A.O. 2003, ApJ, 598, 138

- Kochanek, C.S., Falco, E.E., Impey, C., Lehar, J., McLeod, B. & Rix, H.-W. CASTLeS website, <http://cfa-www.harvard.edu/glensdata/>
- Lauer, T.R., et al. 2005, ApJ, 129, 2138.
- Navarro, J.F., Frenk, C.S. & White, S.D.M. 1996, ApJ, 462, 563
- Navarro, J.F., Frenk, C.S. & White, S.D.M. 1997, ApJ, 490, 493
- Mao, S., Jing, Y., Ostriker, J.P., & Weller, J. 2004, ApJ, 604, L5
- Oguri, M., & Keeton, C.R. 2004, ApJ, 610, 663
- Saha, P. 2000, AJ, 122, 585
- Saha, P. & Williams, L.L.R. 2003, AJ, 127, 2604
- Saha, P. & Williams, L.L.R. 2003, AJ, 125, 2769
- Saha, P. & Williams, L.L.R. 2006, ApJ, 653, 936
- Witt, H.J. & Mao, S. 1997, MNRAS, 291, 211
- Witt, H.J., Mao, S. & Keeton, C.R. 2000, ApJ, 544, 98

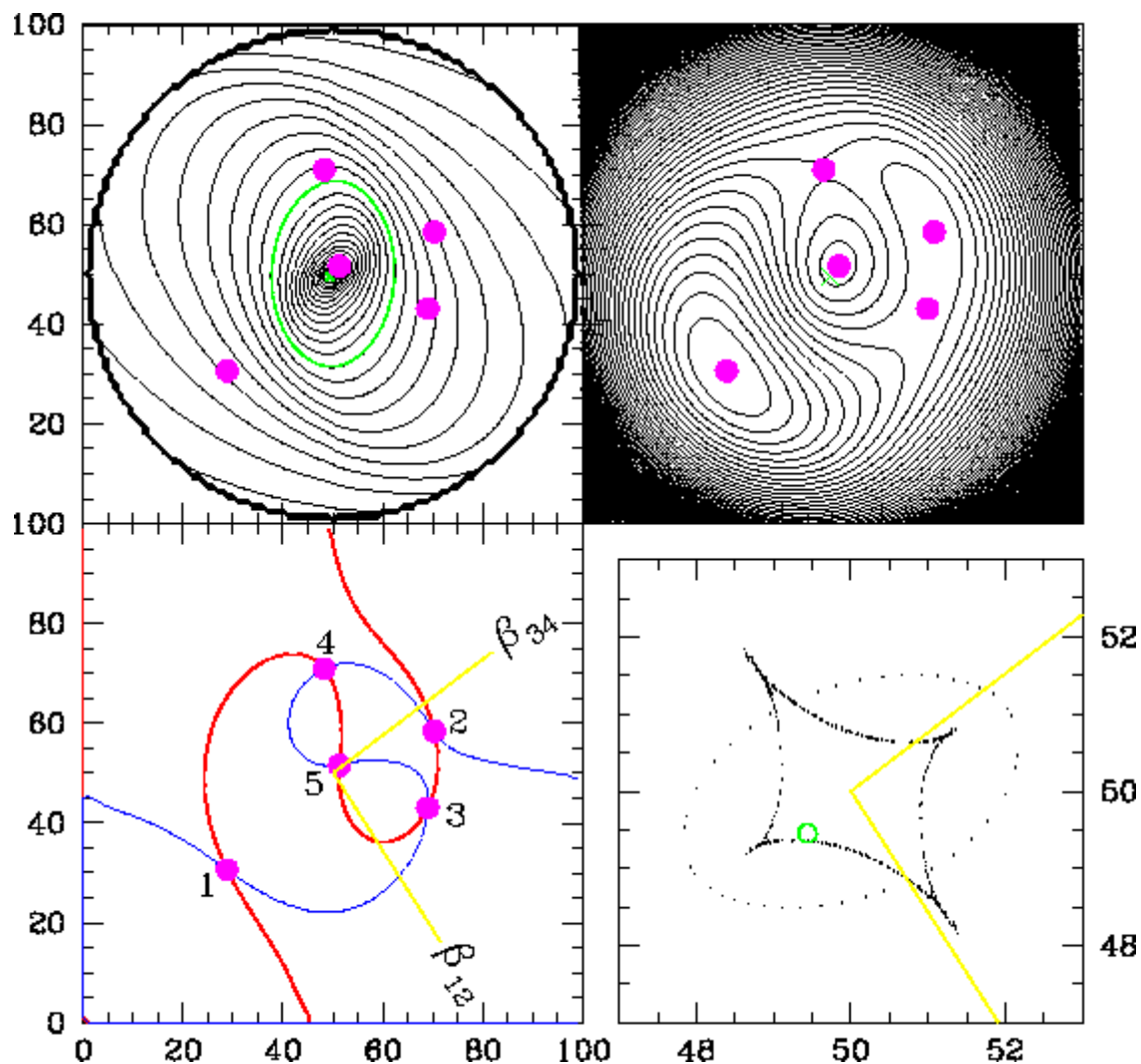


Fig. 1.— A synthetic galaxy lens. *Upper left*: Contours of surface mass density, isodens, of the mass distribution of the lens. The thick (green) contour marks the critical lensing surface mass density. Images are filled (magenta) dots. The contours are spaced linearly. The mass was defined in a circular window. *Upper right*: Arrival time surface, with images. *Lower left*: The thick (red) and thin (blue) lines are the solutions of the lens equation in the x - and y -directions, respectively. The intersections are the image positions. Images are labeled according to the arrival time, from 1 to 5. Two bisector rays, β_{12} and β_{34} are drawn as solid (yellow) lines. *Lower right*: Source plane caustics. The straight lines are the bisector rays. The position of the source is marked with an empty (green) circle.

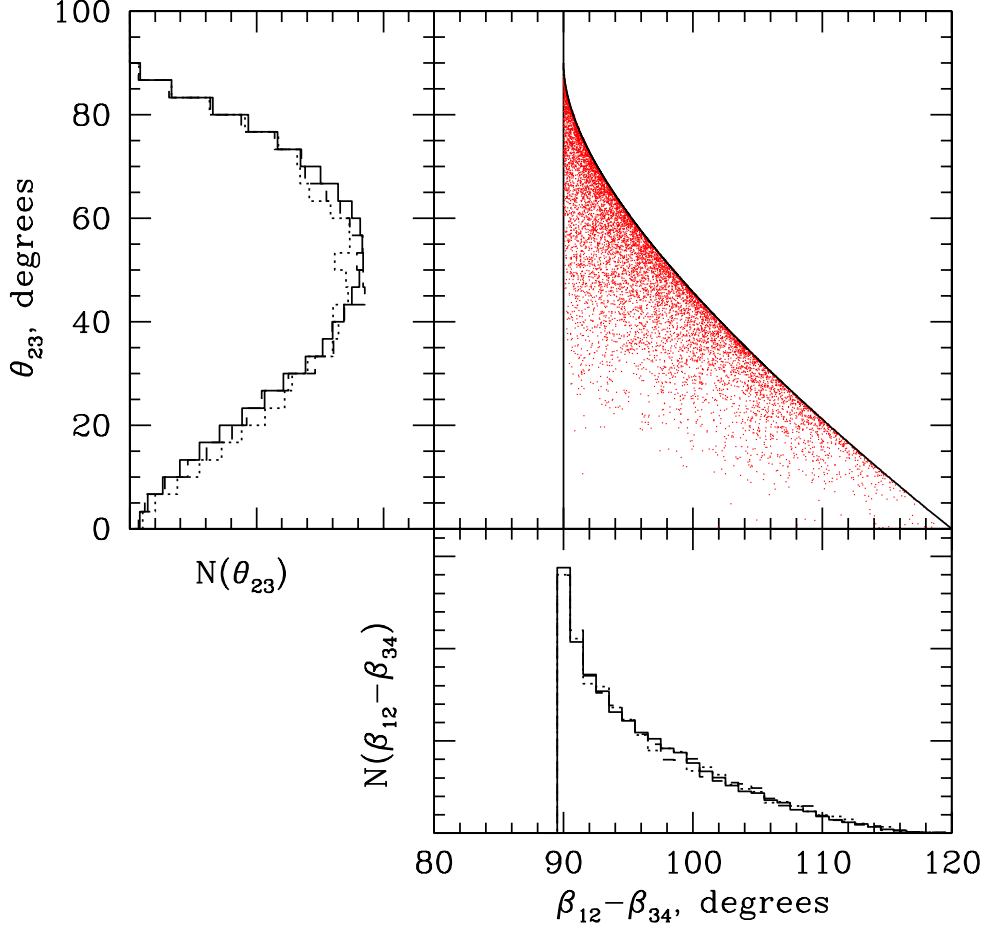


Fig. 2.— The bisector plot for two-fold symmetric lenses as defined in Section 3.1: the difference in bisector angles, $\beta_{12} - \beta_{34}$ vs. the angular separation of images 2 and 3, θ_{23} . Each one of the small (red) points corresponds to a different source location. The pattern of these points, including the upper envelope, appears to be the same for all lenses with two-fold symmetry. The solid curve outlining the envelope is given by eqs. 11 and 9. The left and bottom side panels show the distribution of θ_{23} and $\beta_{12} - \beta_{34}$ respectively. Three different lens models are plotted in the side panels; dashed lines represent a galaxy lens with a shallow non-power law density profile and constant ellipticity of 0.14 (axis ratio 0.75); dotted lines represent an “isothermal” profile, $\propto R^{-1}$ with a small core, and ellipticity of 0.12 (axis ratio 0.79); solid lines represent a circular mass distribution with two external axes of shear, 60° apart, and with shear $\gamma = 0.1$.

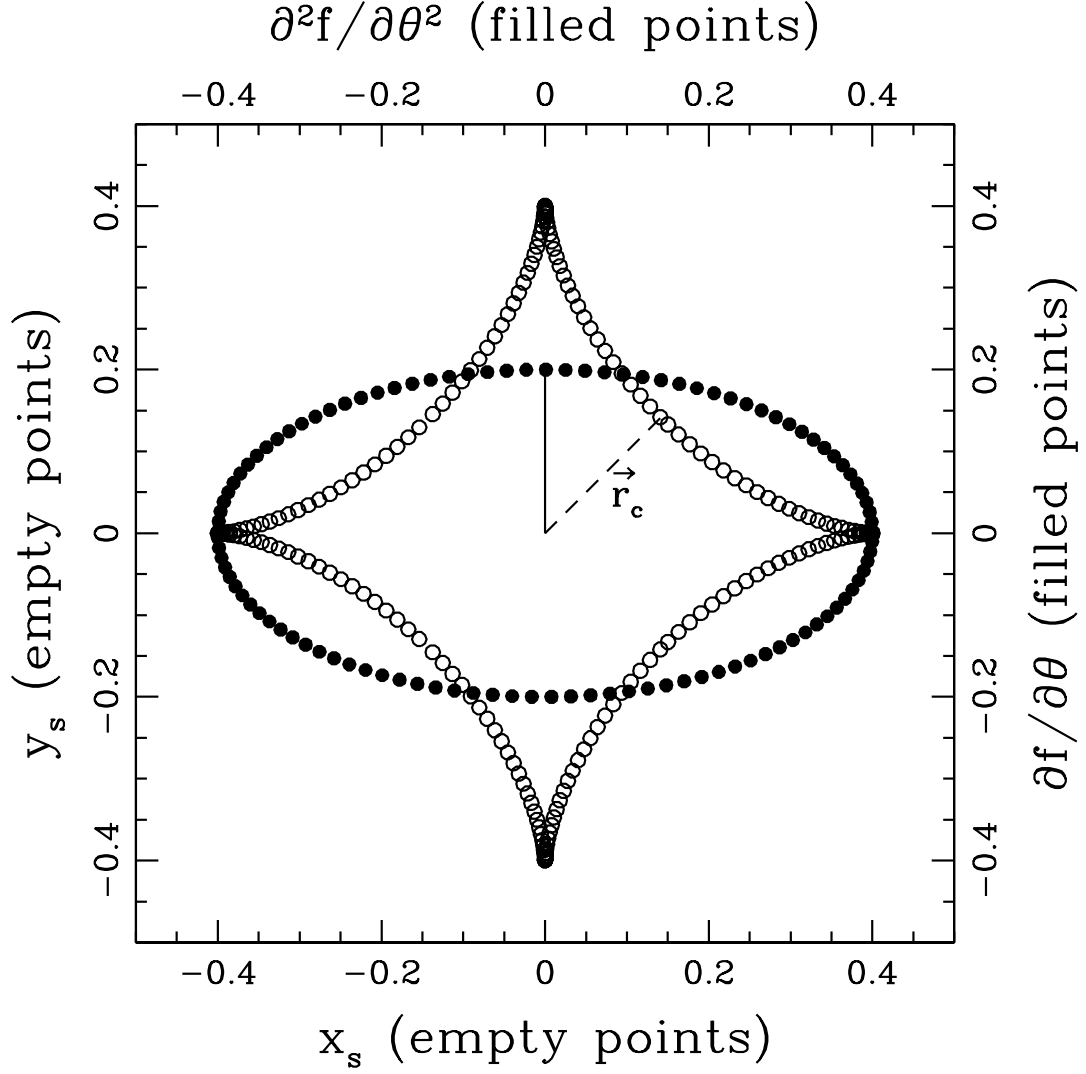


Fig. 3.— The caustic has the usual diamond shape when plotted in the source plane (empty points, and left and lower axes), but when plotted in the plane of $\frac{\partial f}{\partial \theta}$ vs. $\frac{\partial^2 f}{\partial \theta^2}$ (filled points, and right and upper axes) it has an oval shape discussed in Section 3.4. The lensing potential used here is $\phi(r, \theta) = br(1 + \gamma \cos 2\theta)$ with $b = 1$ and $\gamma = 0.1$. The solid line segment represents the point of closest approach in the plane of $\frac{\partial f}{\partial \theta}$ vs. $\frac{\partial^2 f}{\partial \theta^2}$, while the dashed line is \vec{r}_c , in the source plane.

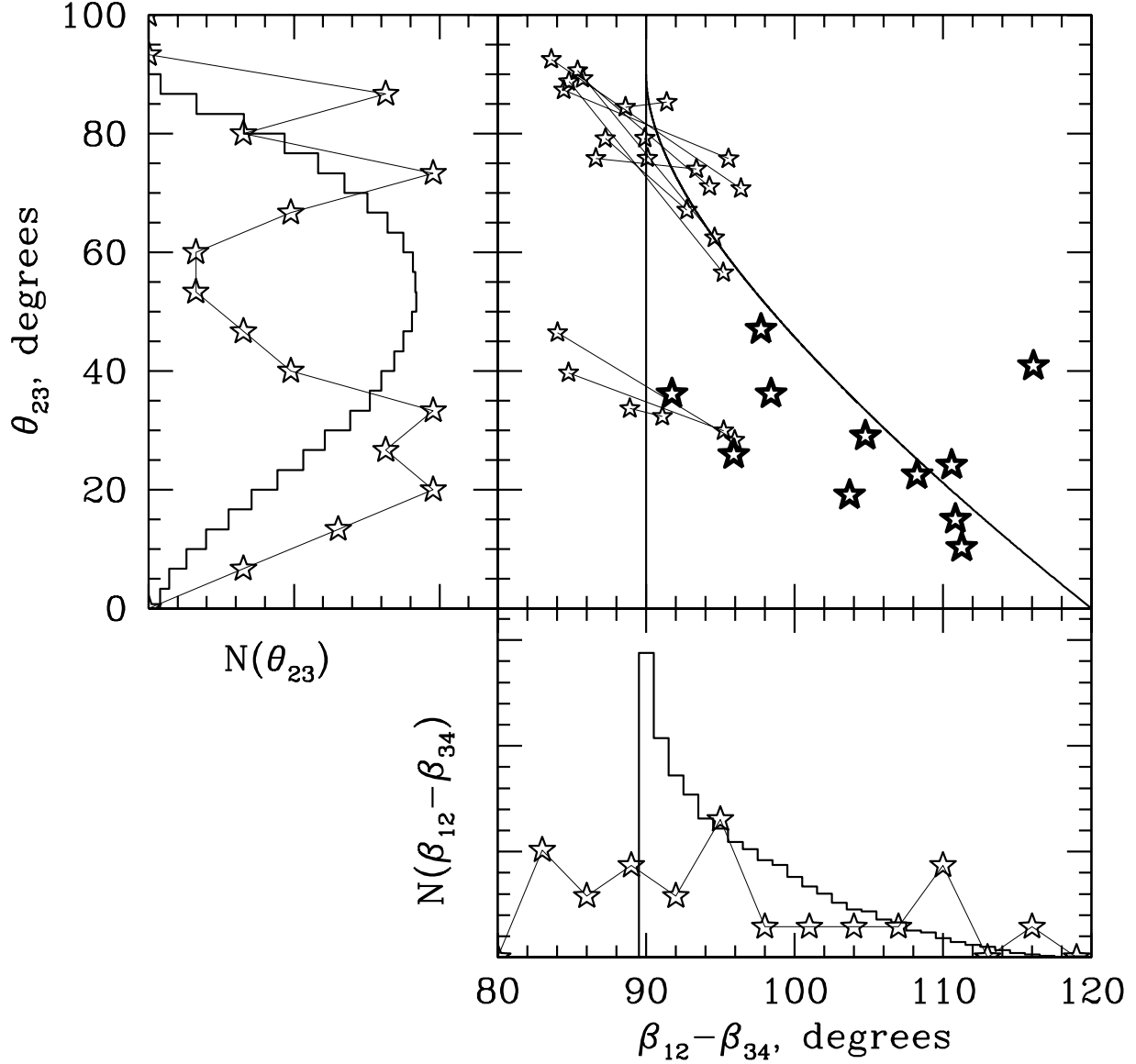


Fig. 4.— Similar to Figure 2. The main portion of the bisector plot shows the real lenses. Quads with unambiguous time ordering (Table 1) are represented by the bold star symbols. The lenses with ambiguous arrival time ordering (Table 2) are shown with two star symbols each, connected by a thin line. The envelope curve is given by eqs. 11 and 9. In the two side panels, the solid line histograms represent two-fold symmetric lenses. The thin line histograms delineated with star symbols represent the data. Each one of the two bisector plane locations of the ‘ambiguous’ lenses was counted as $\frac{1}{2}$ in the histograms.

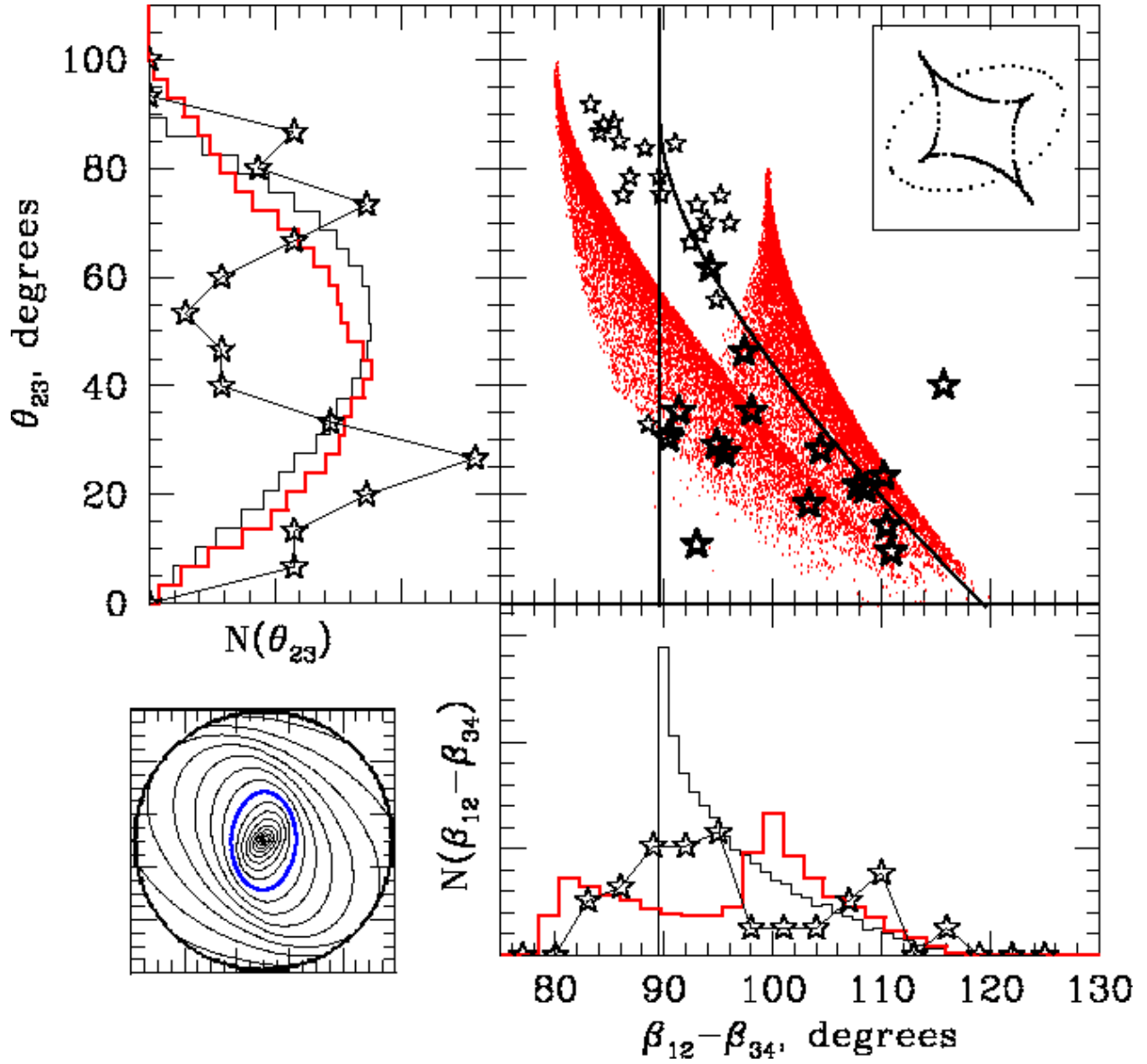


Fig. 5.— Similar to Figures 2 and 4. The isodens of the lens mass distribution are shown in the lower left inset. The thick (blue) contour shows the critical surface mass density for lensing. The contours are spaced logarithmically. (The lens the same as the one shown in Figure 1.) The small (red) points in the main portion of the plot are the quads generated by this lens. The thick (red) line histograms in the two side panels belong to this lens. The thin line histograms are for two-fold symmetric lenses, shown here for comparison. The inset in the upper right shows the source plane caustic.

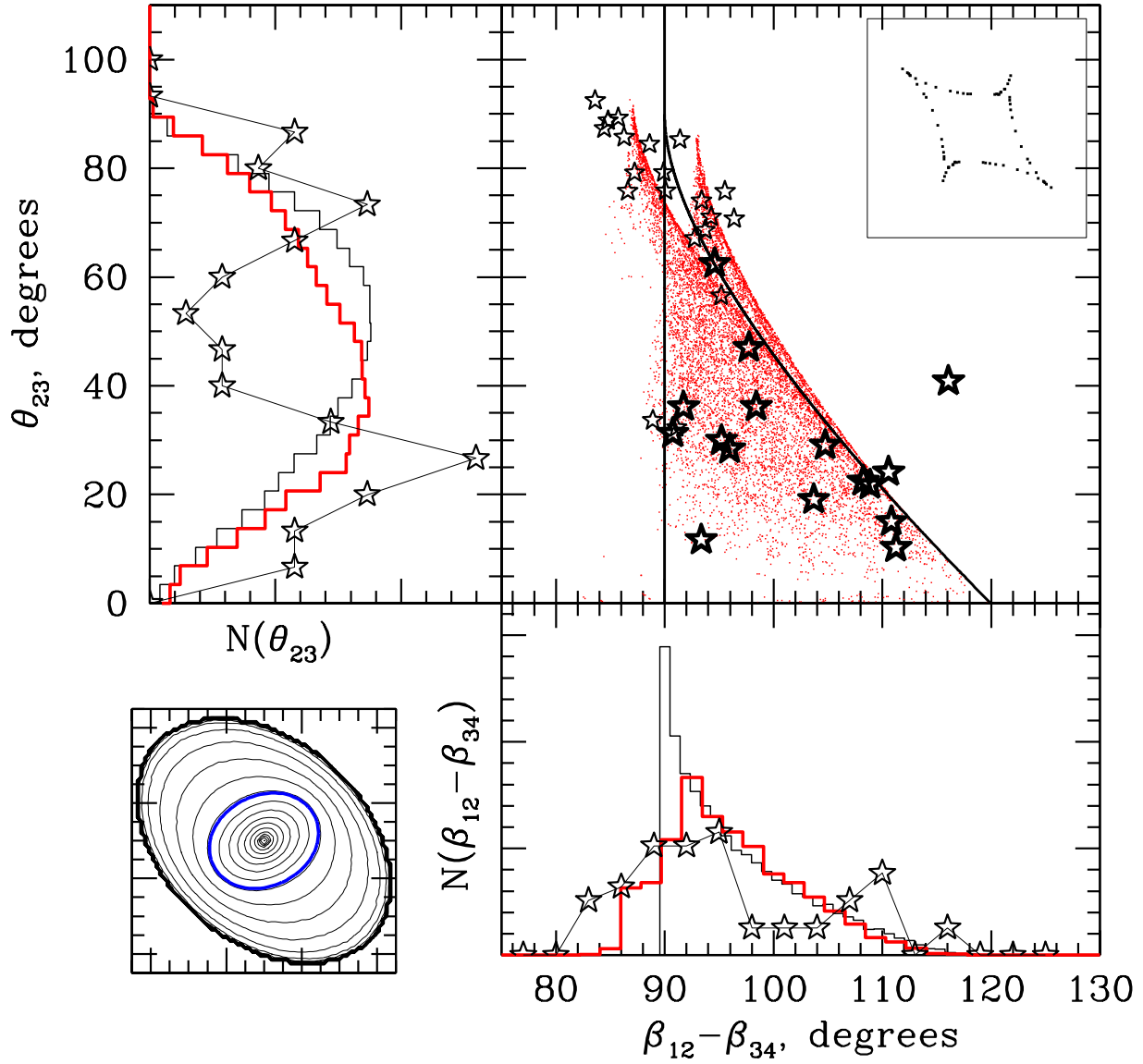


Fig. 6.— Same as Figure 5, only for the lens shown in the lower left. See Section 5 for details.

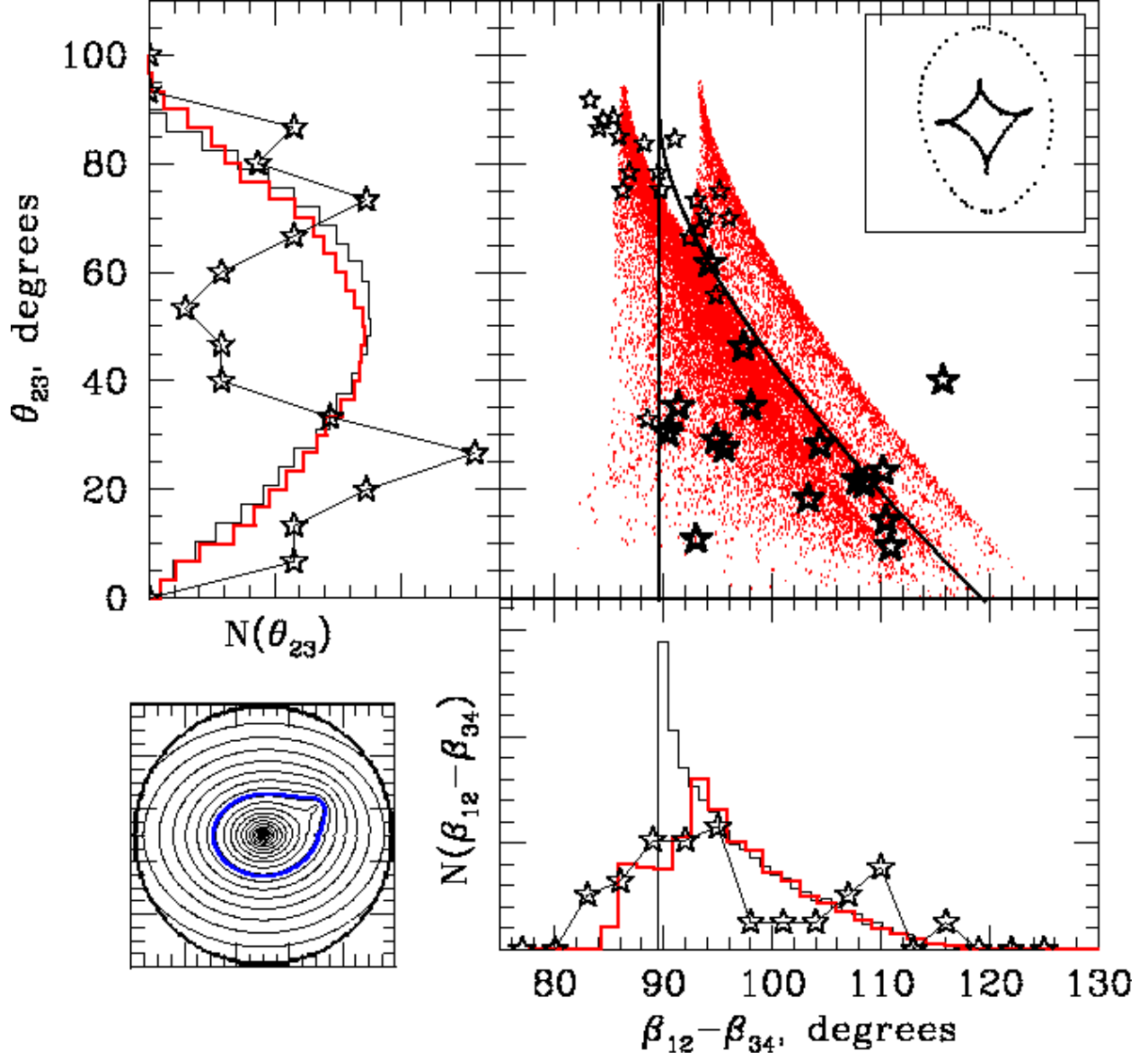


Fig. 7.— Same as Figure 5, only for the lens shown in the lower left. The secondary galaxy comprises about 0.8% of the total lensing mass. The surface density profiles of the main and secondary galaxies are, respectively, $\Sigma_m \propto \exp(-R/R_m)^{0.25}$ and $\Sigma_s \propto \exp(-R/R_s)$, and $R_s/R_m = 0.7$. See Section 5 for details.

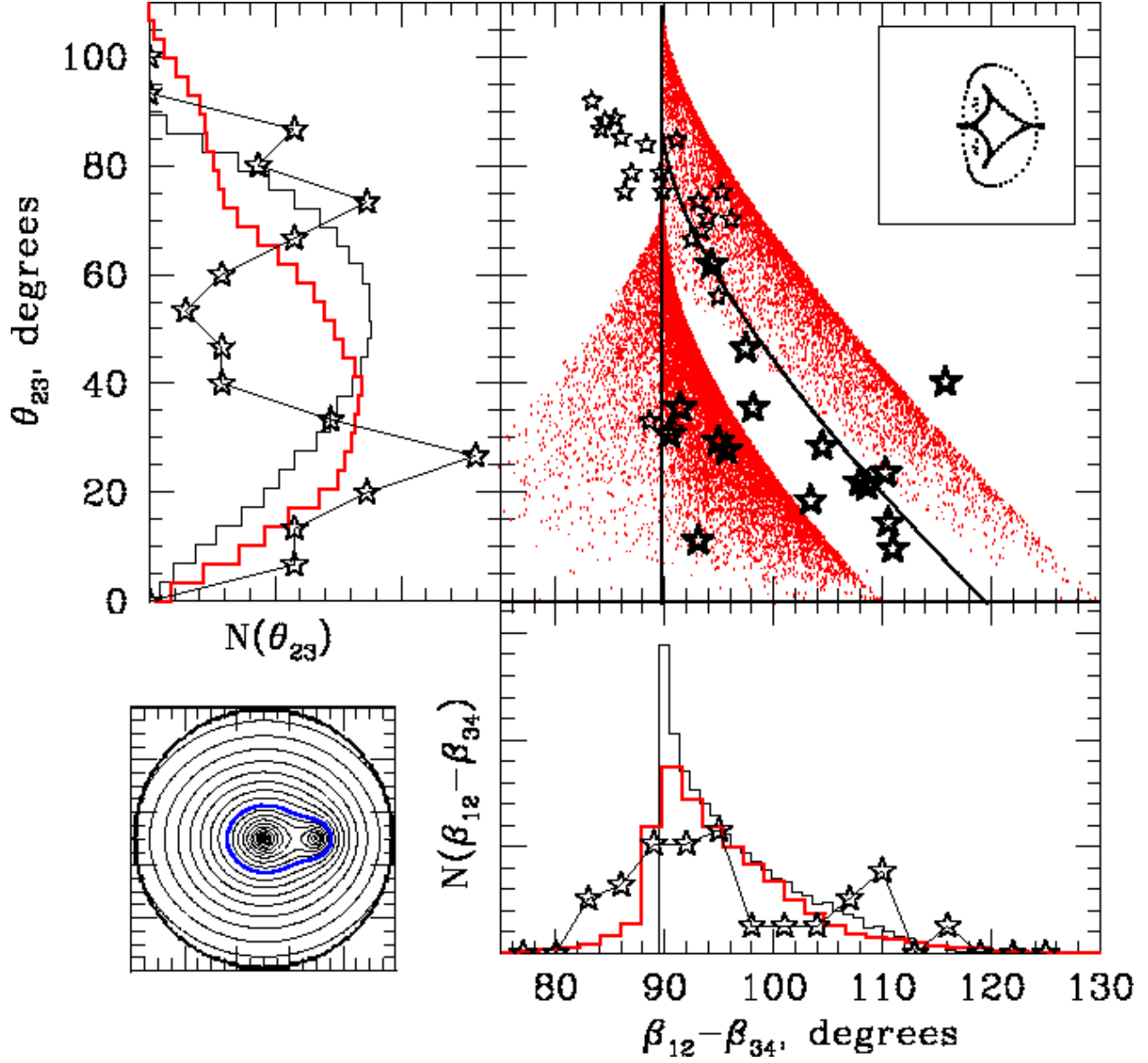


Fig. 8.— Same as Figure 5, only for the lens shown in the lower left. The secondary galaxy comprises about 1.3% of the total lensing mass. The surface density profiles of the main and secondary galaxies are, respectively, $\Sigma_m \propto \exp(-R/R_m)^{0.25}$ and $\Sigma_s \propto \exp(-R/R_s)$, and $R_s/R_m = 0.5$. See Section 5 for details.

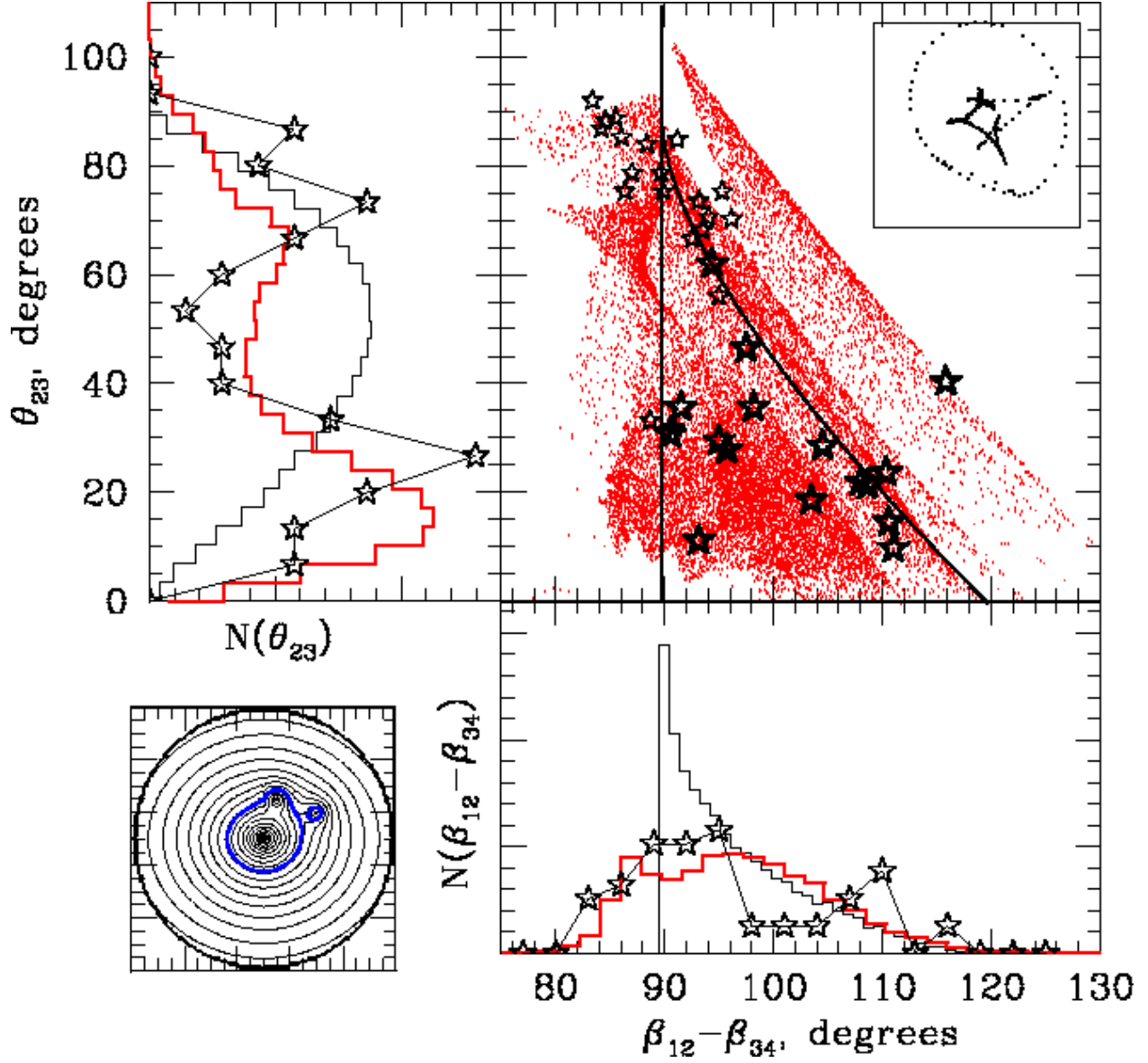


Fig. 9.— Same as Figure 5, only for the lens shown in the lower left. The two secondary galaxies together comprises about 0.4% of the total lensing mass. The surface density profiles of the main and the two secondary galaxies are, respectively, $\Sigma_m \propto \exp(-R/R_m)^{0.25}$ and $\Sigma_s \propto \exp(-R/R_s)$, and $R_s/R_m = 0.2$. See Section 5 for details.

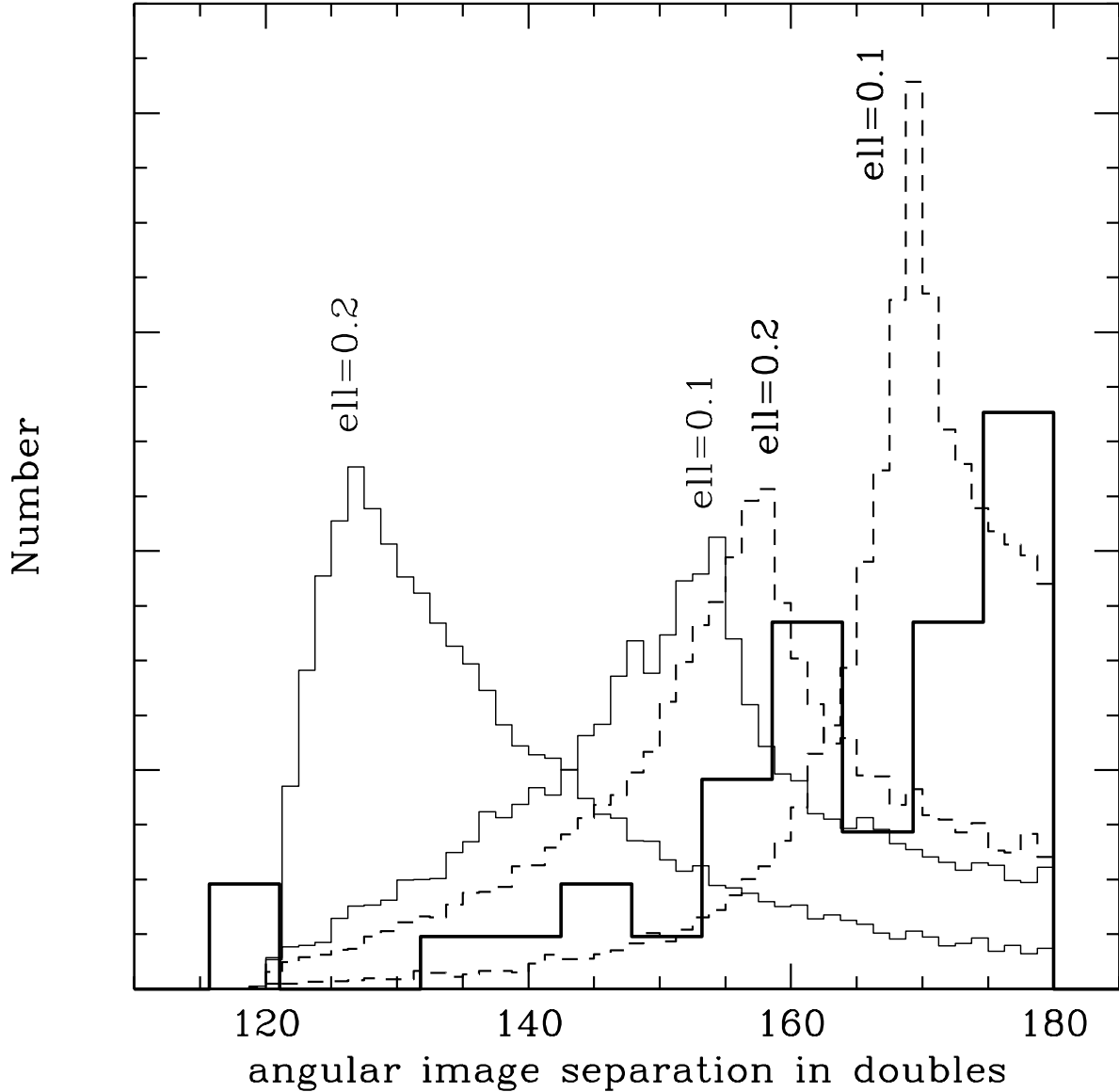


Fig. 10.— The distribution of angles between two images of a double. The thick line histogram shows 39 real doubles. The other four histograms represent synthetic lenses. The two thin solid line histograms correspond to galaxy lenses with projected density profiles $\propto \exp(-R^{0.25})$. The two dashed histograms represent “isothermal”, $\propto R^{-1}$ lenses with a small core. The ellipticities, $e = 0.1$ (axis ratio=0.82) and $e = 0.2$ (axis ratio=0.67) of the lenses are labeled in the plot. See Section 6 for details.

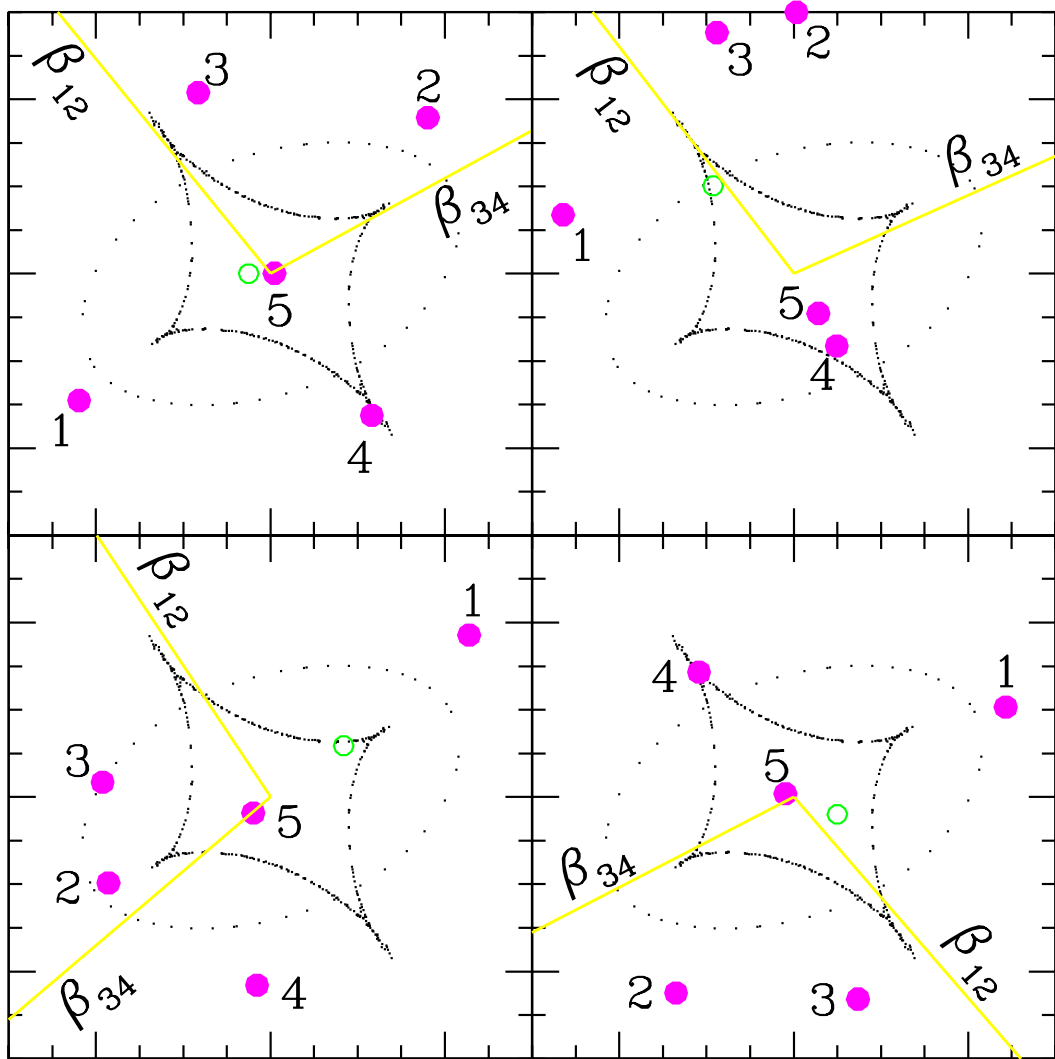


Fig. 11.— All four panels show the caustics of the same lens as in Figure 1, but four different source positions, empty (green) circle. Solid (magenta) dots numbered 1-5 are the *scaled down* positions of images, i.e. angles from the lens center are preserved, but distances are not. The two bisector rays, shown by straight (yellow) lines are labeled in each of the panels.

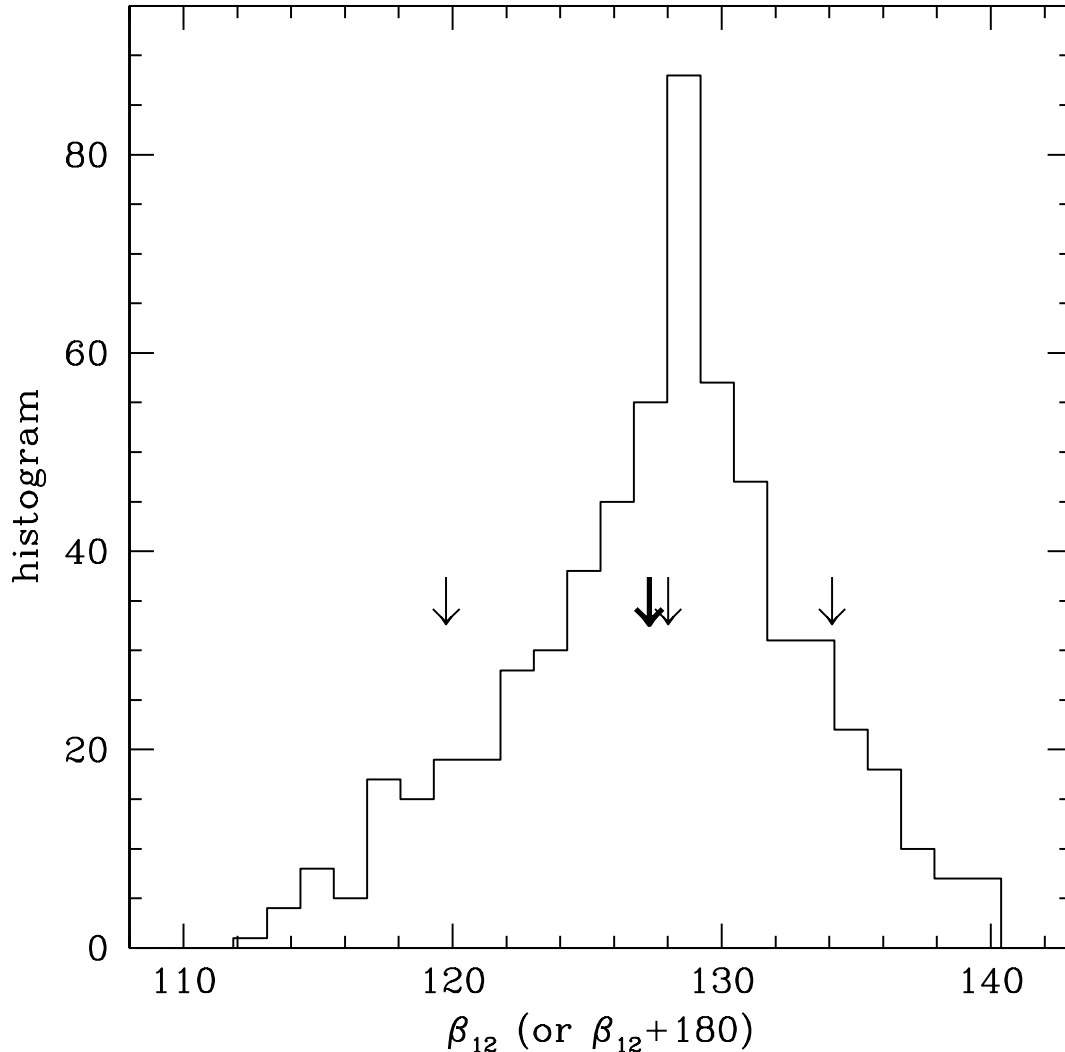


Fig. 12.— The histogram of the PA of the axis containing the bisector ray β_{12} for the lens shown in Figures 1 and 11. Each source position contributes one value to the histogram. The thick arrow indicates the *actual* PA of the major axis of the diamond caustic. The actual PA is very nearly the same as the mode and the median (central thin arrow) of the β_{12} distribution. The other two thin arrows mark the 10th and 90th percentiles. The plot illustrates that the PA of the axis containing the bisector ray β_{12} coincides, to within a few percent, with the major axis of the diamond caustic, and hence the major axis of the lens’ mass ellipticity in the image circle. See Section A for details.

Table 1. Lens with unambiguous arrival time ordering

$\beta_{12} - \beta_{34}$	θ_{23}	Lens name
103.71	19.08	MG0414+0534
110.59	24.13	PG1115+080
116.09	40.85	HE0230-2130
97.74	47.00	SDSS0924+0219
111.27	10.25	B0712+472
108.25	22.46	HS0810+2554
110.84	15.01	B1933+503 (lobe)
104.77	29.05	WFI2026-4536
98.41	36.14	WFI2033-4723
91.74	36.11	B1608+656
95.23	29.95	RXJ0911+0551
90.76	31.25	SDSSJ125107
108.89	21.79	B1555+375
94.61	62.47	SDSS1138+0314
95.97	28.37	B1422+231
93.38	11.66	B2045+265

Table 2. Lens with ambiguous arrival time ordering

$\beta_{12} - \beta_{34}$	θ_{23}	Lens name
91.10	32.34	RXJ1131-1231
88.90	33.67	“
93.39	74.05	HST12531-2914
86.61	75.83	“
84.80	88.77	B1933+503 (core)
95.20	56.57	“
91.39	85.29	SDSS1011+0143
88.61	84.44	“
85.73	89.28	H1413+417
94.27	71.07	“
95.55	75.77	HST14176+5226
84.45	87.34	”
96.39	70.73	HST14113+5211
83.61	92.51	“
87.24	79.19	Q2237+030
92.76	67.11	“
90.09	75.88	HE0435-1223
89.91	79.25	“
93.72	68.65	HE1113-0641
86.28	85.76	“